Piezotronics and piezo-phototronics based on *a*-axis nano/microwires: fundamentals and applications

2017 Semicond. Sci. Technol. 32 043005

(http://iopscience.iop.org/0268-1242/32/4/043005)

IOP Publishing Semiconductor Science and Technology
Semicond. Sci. Technol. **32** (2017) 043005 (16pp) https://doi.org/10.1088/1361-6641/aa5fcd

Topical Review

Piezotronics and piezo-phototronics based on *a*-axis nano/microwires: fundamentals and applications

Xingfu Wang[1], Wenbo Peng[1], Caofeng Pan[2] and Zhong Lin Wang[1,2]

[1] School of Materials Science and Engineering, Georgia Institute of Technology, Atlanta, GA 30332-0245, United States of America
[2] Beijing Institute of Nanoenergy and Nanosystems, Chinese Academy of Sciences; National Center for Nanoscience and Technology (NCNST), Beijing, 100083, People's Republic of China

E-mail: zhong.wang@mse.gatech.edu

Received 17 December 2016, revised 6 February 2017
Accepted for publication 10 February 2017
Published 24 March 2017

Abstract

One-dimensional semiconductors with wurtzite structure, such as GaN, ZnO and CdS nano/microwires, exhibit superior semiconductor, piezoelectric and mechanical properties, making them excellent candidates for novel electronic, opto-electronic devices and integrated systems. More importantly, the coupling between piezoelectric polarization and semiconductor properties (including electric transport and photoexcitation) gives rise to unique and unprecedented physical characteristics and has led to emerging fields of piezotronics and piezo-phototronics. On the basis of the extensive studies in *c*-axis semiconductor nano/microwires, piezotronics and piezo-phototronics based on *a*-axis nano/microwires have further been explored and demonstrated recently. We review both the fundamental progresses and developed applications of piezotronics and piezo-phototronics based on *a*-axis nano/microwires, which further improve the theoretical framework and expand the practical applications of piezotronics and piezo-phototronics in functional nanodevices and nanosystems.

Keywords: 1D semiconductors, piezotronics, piezo-phototronics, *c*-axis, *a*-axis, nano/microwires

(Some figures may appear in colour only in the online journal)

1. Introduction

Piezoelectricity is a well-known phenomenon that involves a polarization potential under mechanical deformation (squeezing, twisting, stretching, compression or bending) in certain materials without inversion symmetry [1–3]. Over the past several decades, this effect has been deeply investigated based on bulk materials, planar structures and nanostructures for various functional applications, such as sensors [4, 5], actuators [6, 7], switches [8, 9], integrated microelectromechanical systems (MEMS) [10] and energy harvesters [11, 12]. The most common semiconductor materials with piezoelectricity, such as quartz, $Pb(Zr_xTi_{1-x})O_3$ (PZT) and poly(vinylidene fluoride) (PVDF), are almost electric insulators with few free carriers, and, thus, less useful for functional electronics and building blocks/components [13]. In piezoelectric semiconductor materials, mechanical-deformation-induced piezoelectric polarization and corresponding piezoelectric polarization charges (*piezo-charges*), can effectively tune/control the distribution and transport properties of the charge carriers in the semiconductors; this is the piezotronic effect [14–16]. The piezo-phototronic effect [14, 15] is a three-way coupling effect among piezoelectric polarization potential (*piezo-potential*), semiconducting properties and photoexcitation. Optoelectronic processes of charge carriers within semiconductors, such as generation, transport, separation and

recombination, can be controlled/tuned by introducing piezo-charges created and presented at the local interface.

Low dimensional wurtzite-structured piezoelectric semiconductors, such as ZnO and GaN nano/microwires, have attracted considerable attention in electronics, optoelectronics and integrated circuits owing to the co-existence of semiconductor, piezoelectric and superior mechanical properties. The preferential polar growth direction of one-dimensional (1D) wurtzite semiconductors are typically along *c*-axis caused by the instability and high surface activities of the polar (0001) plane [17]. The piezotronics and piezo-phototronics based on *c*-axis nano/microwires have been extensively explored for a wide range of applications in strain-gated transistors [18], logical computations [19], optimizing the performances of chemical/bio-/photosensors [20, 21], improving the efficiency of light emitting diodes [22, 23], solar cells [24], etc. On the basis of these achievements, piezotronics and piezo-phototronics in nonpolar *a*-axis semiconductor nano/microwires are further developed recently, considering the generation and distribution of piezo-potential and piezo-charges are closely related to crystallography, such as crystal orientation. This review outlines the fundamental principles, recent progress and promising future applications of the piezotronics and piezo-phototronics based on *a*-axis nano/microwires.

2. Basics of piezotronics and piezo-phototronics

2.1. Piezoelectric polarization and piezopotential

Owing to non-center symmetric crystal structure of the wurtzite semiconductors (ZnO, GaN, InN, and CdS), piezoelectric polarization is created within the crystal along certain orientations once upon a static mechanical straining. For example, from a microscopic point of view, hexagonal structured ZnO has anisotropic properties in the directions along and perpendicular to the *c*-axis [25]. The Zn^{2+} cations and the O^{2-} anions in a unit cell are tetrahedrally coordinated, and the centers of positive charges and negative charges overlap with each other under equilibrium. Once an external stress is applied to ZnO along its *c*-axis, a relative displacement between the center of cations and anions occurs. As a result of the Zn^{2+} cations and the O^{2-} anions sitting off-center inside the crystal, the unit cell is effectively turned into an electric dipole moment (figure 1(a)). In a macroscopic crystal, the piezo-potential is created along the straining direction (figure 1(b)) because of the constructive add-up of the electric dipole moments in each unit cell that comprises the crystal structure [26, 27]. Therefore, the piezo-charges are induced and presented at the vicinity of the $+c$ and $-c$ end of the crystal. The generated piezo-potential/charges allow the redistribution and/or transport-behavior modulation of the free carriers inside the crystal. Thus, the electric and/or optoelectronic processes/behaviors will then be controlled/tuned across the local contact, which gives rise to the new field of piezotronics and piezo-phototronics [28] (figure 2).

3. Piezotronics and piezo-phototronics

3.1. The piezotronic effect on M–S and p–n junctions

The origins and fundamental principles of the piezotronics and piezo-phototronics can be traced back to 2007, which were discovered and conceived by Wang [29]. Owing to the coupling between semiconductor and piezoelectric properties, the piezo-potential is induced by external strain within the piezoelectric semiconductor along its polar direction, and the piezo-charges are created and presented at the surfaces of semiconductor or at the local interface formed with other materials [30, 31]. By utilizing the piezo-charges to redistribute the charge carriers inside the semiconductor and modulate the energy band at local contact or junction, the transport behavior/electric process of the free carriers can be modulated/tuned, which is referred to as the piezotronic effect. Further, the piezo-phototronic effect is introduced as a three-way coupling between piezo-potential, semiconductor properties and photoexcitation by applying piezo-charges at the vicinity of the local interface to modulate the optoelectric processes of charge carriers, such as generation, separation, transport and recombination, within the piezoelectric semiconductors [32–38]. These two emerging effects, in the past several years, have attracted tremendous interest worldwide and been demonstrated in many semiconductors fundamentally and also been explored for various applications in functional devices.

A Schottky barrier between a metal electrode and semiconductor (M–S) is formed as a result of the difference between the metal–vacuum work function and the semiconductor–vacuum electron affinity [39]. The piezo-charges presented at the vicinity of the semiconductor side have a significant influence on the Schottky barrier height (SBH) [26, 27, 40, 41]. If the *c*-axis of the semiconductor points to the metal electrode, upon compressive strain, the negative piezo-charges are created at the semiconductor side contacting with the metal (upper panel, figure 3(a)). The non-mobile negative piezo-charges repel the majority (i.e. electrons here) in semiconductor and widen the depletion region at this side, thus increasing the local SBH. Alternatively, the local interface of the semiconductor becomes less depleted by the tensile-strain-induced positive piezo-charges, resulting in a lower SBH (upper panel, figure 3(a)). Therefore, external-strain-induced piezo-potential and piezo-charges can effectively modulate the electric transport behaviors of the M–S Schottky contact.

As one of the most common components for optoelectronic applications, if a p–n junction is composed of piezoelectric semiconductor, the ionized charges in depletion region of the p–n junction can effectively couple with the piezo-charges [22, 42, 43]. As a result, the properties of the

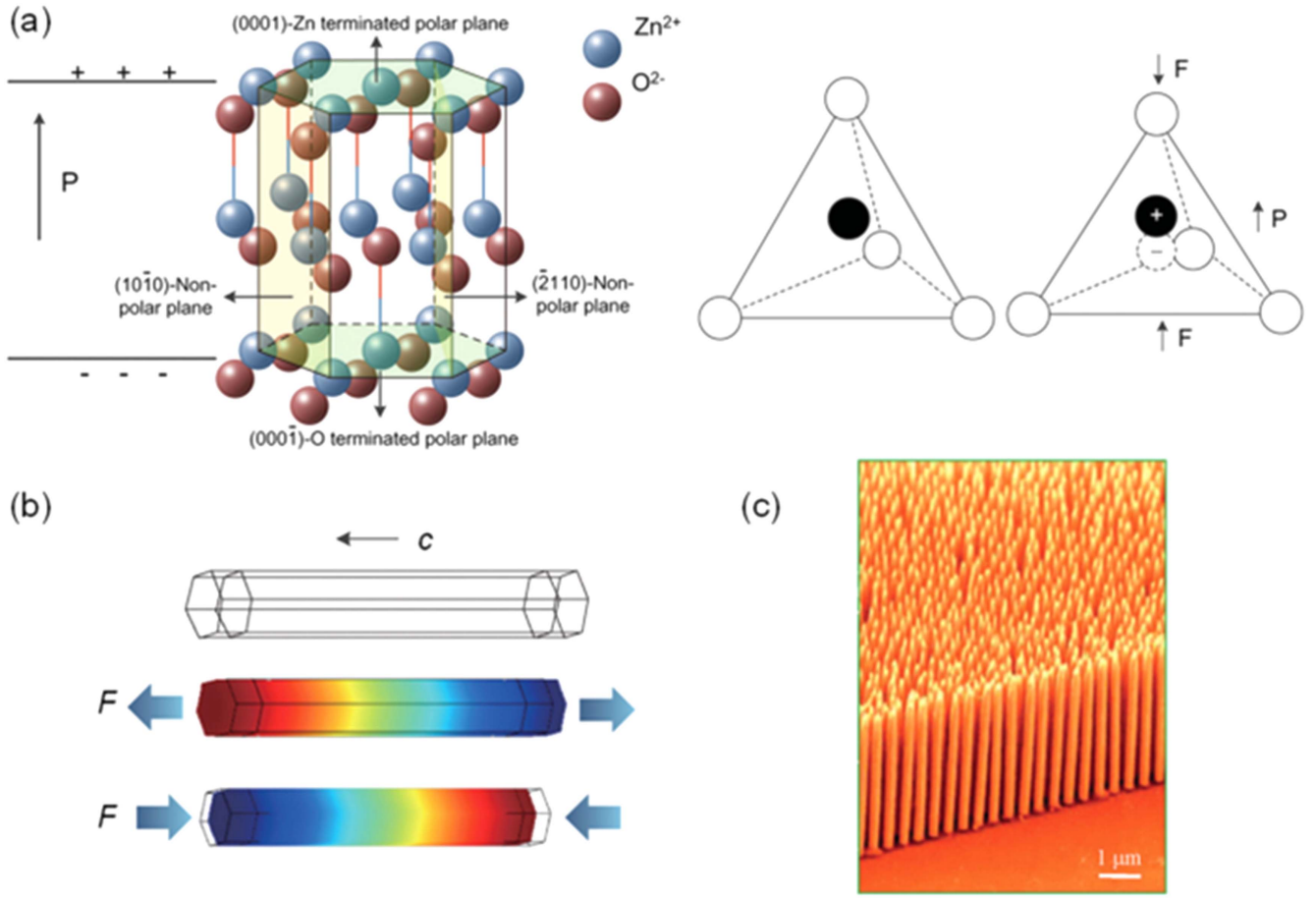

Figure 1. Piezo-potential in a wurtzite crystal. (a) Atomic model of the wurtzite-structured ZnO [14] John Wiley & Sons. [© 2012 WILEY-VCH Verlag GmbH & Co. KGaA, Weinheim]. (b) The distribution of piezopotential along a ZnO nanowire (NW) under axial strain calculated by numerical methods. The growth direction of the NW is along the *c*-axis. The color gradient represents the distribution of piezo-potential in which red indicates positive piezo-potential and blue indicates negative piezo-potential. Reprinted from [27], with the permission of AIP Publishing. (c) Aligned ZnO-nanowire arrays by a solution-based approach. [28] (2012) (© Springer-Verlag Berlin Heidelberg). With permission of Springer.

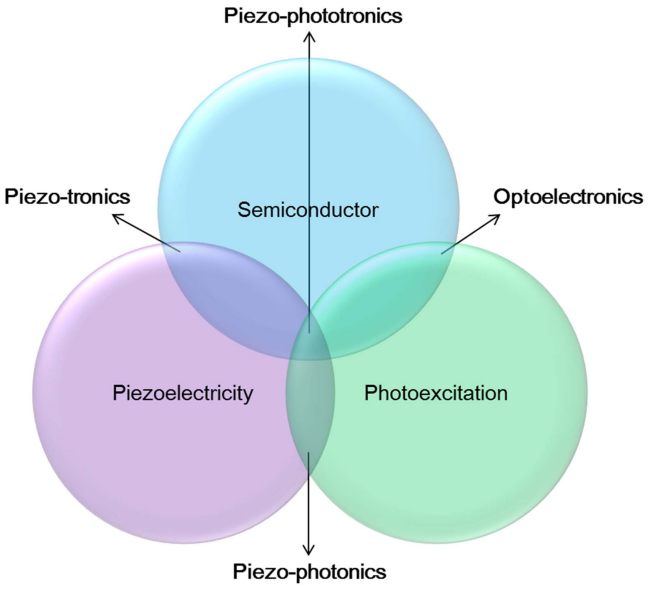

Figure 2. Coupling among piezoelectric, optical and semiconducting properties in piezoelectric semiconductor materials is the basis of piezotronics (piezoelectricity–semiconductor coupling), piezophotonics (piezoelectricity–photoexcitation coupling) and piezo-phototronics (piezoelectricity–semiconductor–photoexcitation coupling).

depletion region (the potential barrier height and energy band profile) are significantly influenced. In the case of a p–n homojunction with an n-type piezoelectric semiconductor, the piezo-charges are produced at the side of n-type semiconductor under external straining. The induced piezo-charges can affect the depletion region width and local band alignment at the junction region, and modulate the redistribution of the charge carriers and corresponding electric transport behavior in the p–n junction. If the $+c$ direction of the n-type semiconductor points to the p-type component, the negative piezo-charges induced by compressive strain can attract majority holes within p-type semiconductor and repel free electrons in n-type region, giving rise to the modulated depletion region of the p–n junction, which shifts the total depletion region towards n-side. More importantly, a local upward energy band bending is caused due to the existence of the negative piezo-charges (upper panel, figure 3(c)). By contrast, under tensile strain condition, the total depletion region shifts towards p-side and the local energy band bends downward arise from the induced positive piezo-charges located at the vicinity of the junction region (upper panel, figure 3(d)). Owing to the modulations of depletion region and corresponding energy band profile of p–n junction by

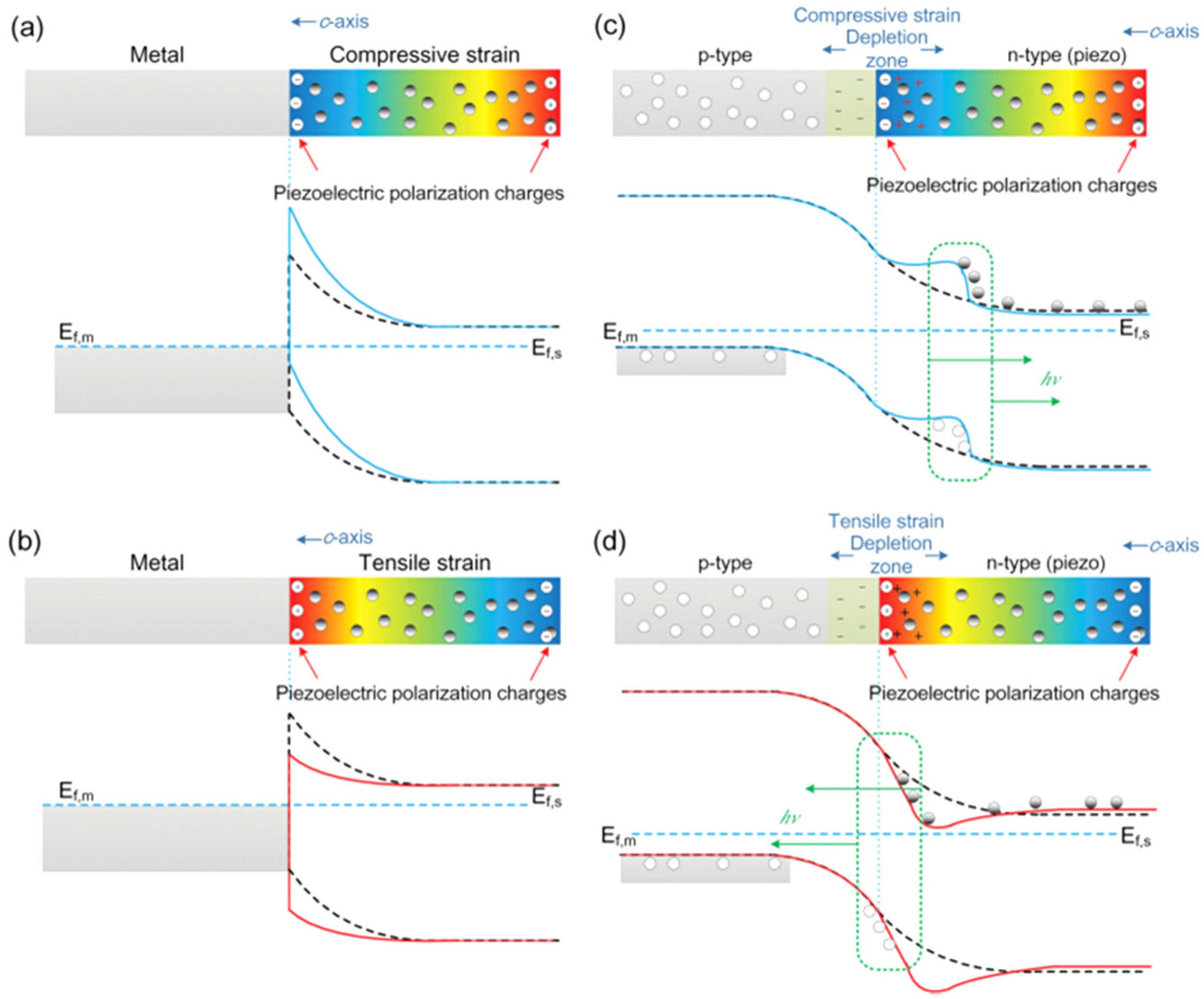

Figure 3. Schematic of the energy band diagram illustrating the piezo effect on the M–S interface and piezo-phototronic effect on p–n junction interface. (a) Negative polarization charges are induced at the interface, increasing the barrier height. (b) Positive polarization charges are induced at the interface, decreasing the barrier height. (c) Negative polarization charges are induced at the interface, creating a bump in the band diagram. (d) Positive polarization charges are induced at the interface, creating a dip in the band diagram. For the color gradient, red represents positive potential and blue represents negative potential. (a)–(d) [23] John Wiley & Sons. [© 2015 WILEY-VCH Verlag GmbH & Co. KGaA, Weinheim].

piezo-potential and piezo-charges, the electric processes in corresponding electronic devices are therefore effectively modulated.

3.2. The piezo-phototronic effect on M–S and p–n junctions

External strain-induced piezo-polarization and interfacial piezo-charges can effectively modulate the generation, separation, transport and recombination of free charge carriers in optoelectronic devices based on piezoelectric semiconductors. The piezo-phototronic effect is known as a three-way coupling among piezoelectricity, semiconductor properties and photoexcitation. The piezo-phototronic effect in Schottky contacted photodetector, typically involving the generation, separation and transport of photogenerated carriers, is firstly discussed. Incident-photons produce non-equilibrium electron–hole pairs in the piezoelectric semiconductor. Under strain-free condition, the electron–hole pairs are separated by the internal electric field at the local M–S junction and then collected by the metal electrodes, giving rise to a photocurrent. The separation and transport behaviors of electrons and holes are critically dependent on the barrier characteristics, such as the SBH [44]. If positive piezo-charges induced by the external strain are created at the vicinity of the local interface of the reversely biased Schottky junction, the SBH decreases and corresponding re-aligned energy band profile can effectively separate and/or redistribute of holes and electrons. Simultaneously, the potential barrier for the positively biased Schottky contact is increased. Consequently, the separation and collection of photon-induced non-equilibrium carriers within the device is suppressed. If negative piezo-charges are induced at the reversely biased Schottky

junction, the SBH increases and corresponding energy band profile promotes the separation, transport and collection of the photo-generated electrons and holes. However, when the density of induced negative piezo-charges at the reversely biased Schottky junction is large enough, strong upward bending of the valence band edge can create a new energy barrier for hole transport. Therefore, holes are trapped at the local interface, which hinders the separation of photo-excited electron–hole pairs. The related re-alignment of the conduction band can increase the dark current due to the enhanced tunneling events, and thus deteriorates the photoresponse performances of the photodetectors.

The photoresponse in a p–n junction is attributed to the separation and collection of the photo-induced electron–hole pairs through band-to-band optical transitions. The photo-induced charge carriers are separated and transported from the depletion region by the internal built-in electrical field towards the n- and p-type bulk regions, respectively, leading to the photocurrent. When the positive piezo-charges are created within the n-type region, the expansion and shift of the space charge region towards the p-type region can increase the effective series resistance for charge injection to the contact and hence decrease the device current. Furthermore, the formation of a charge channel in the conduction band and the corresponding downward bending of the valence band edge on the n-type region lead to less-effective separation of the electron–hole pairs. On the contrary, if the negative piezo-charges are created and presented at the junction in the n-type region, the expansion and shift of the depletion region towards the n-type side decrease the effective series resistance for charge injection to the contact and hence increase the device current. Moreover, the corresponding upward band bending can suppress electron–hole recombination and allow effective separation of the photo-generated carriers.

4. Axial orientation dependence of piezotronics and piezophototronics

4.1. c-axis piezotronics and piezophototronics: interfacial effect

Wurtzite semiconductor nano/microwires with polar *c*-axis orientation are ideal candidates for piezotronic and piezo-phototronic applications, owing to their excellent stress/deformation tolerance and large polarity along or perpendicular to *c*-axis. The piezo-potential is created along the polar *c*-axis and the piezo-charges are induced and located at the vicinity of the semiconductor nano/microwires end faces. To achieve a uniform Fermi level under equilibrium, M–S Schottky junction or homo-/heterojunction is formed when the semiconductor nano/microwires contact with metal or other semiconductor materials. The space depletion region is created at the interface when the two components of a junction contact with each other due to the diffusion of majority and drift of minority. The resistance of the junction region is extremely high due to the carrier depletion while the resistances of n-type and p-type region beyond junction region are very low owing to the existence of large amount of majority, leading to that the external applied voltage falls mainly in the junction/depletion region [39]. Therefore, the physical characteristics of the depletion region, such as the depletion width and barrier height, are crucially important to the electric and photoelectric processes in electronic and optoelectronic applications. If the M–S Schottky junction or homo-/heterojunction are formed at one end of a *c*-axis nano/microwire, the piezo-charges created and presented at local interface of this end under external deformation can significantly influence the depletion width and barrier height and hence effectively control/tune the electric and photoelectric behaviors of the charge carriers. Therefore, the piezotronic/piezo-phototronic effects in *c*-axis nanostructures are interfacial effects, which utilize the piezoelectric polarizations created at the local M–S contact or homo-/hetero-junction located at the local interface/end of the nanostructures to control the carriers transport across the interface and corresponding optoelectronic processes of the photo-induced charge carriers [23, 45].

4.2. a-axis piezotronics and piezophototronics: volumetric and interfacial effect

Wang *et al* have proposed a single NW piezoelectric field-effect transistor (PE-FET) based on *a*-axis nano/microwire model [29]. By fabricating an M–S–M Schottky contact device using a single NW on a flexible substrate, a bending force can be effectively applied upon the NW. The piezoelectricity-induced electric field across the bent NW can acts as a 'gate' to control the electric current transport behavior within the NW (figure 4(a)). Once an n-type NW is subject to an externally static stress, a piezo-potential is created across the width of the NW, leading to trapping of the free electrons at the surface of the positive piezo-charge side. This can effectively reduce the carrier concentration within the NW. On the other side, the negative piezo-charges induced by external strain can repulse away the free electrons, and thus a charge depletion zone can be formed near the negative piezo-potential side. Consequently, the effective conducting-channel width of the single NW is reduced caused by the formation of the depletion region. Therefore, the piezo-potential across the width of the NW induced upon external straining can serve as an electric field to tune/control the electric transport properties of the NW devices, which is equivalent to a gate voltage applied on the gate dielectric in the traditional voltage-triggered NW FET. A piezoelectric (PE)-gated diode has also been demonstrated simultaneously. The PE-diode is different from the PE-FET discussed above because only one side of the bent NW is in contact with the probe. The stationary end of the NW is fixed at one probe, while the other probe bends the NW from the tensile side (figure 4(b)).

According to the *a*-axis nano/microwire model discussed above, apparently different from the piezotronics and piezo-phototronics in *c*-axis based piezoelectric semiconductor materials, the *a*-axis piezotronics and piezophototronics are mainly the volumetric and interfacial effects. The underlying physical mechanism of the piezotronic effect of *a*-axis piezoelectric semiconductor (*a*-axis GaN nanobelt) under

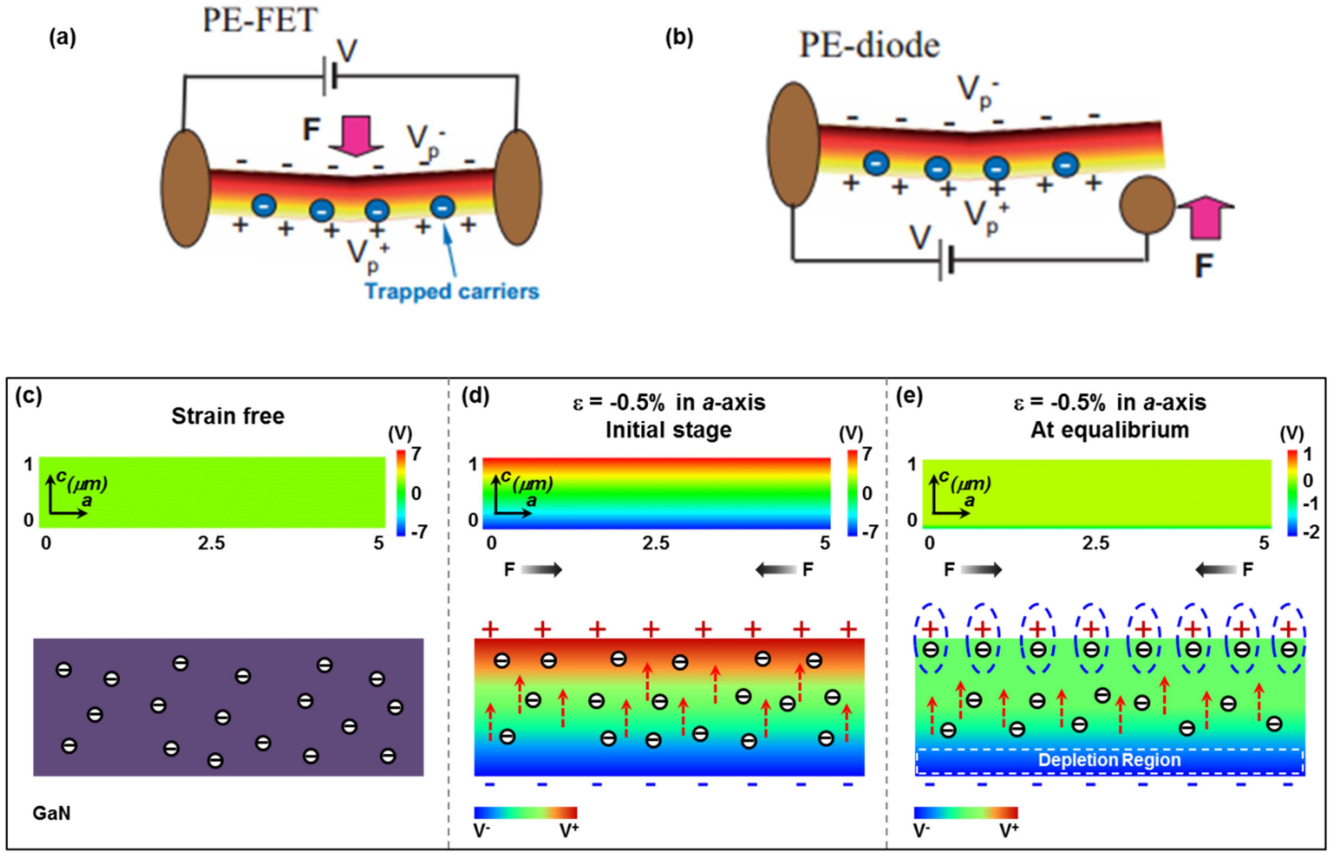

Figure 4. Physical mechanisms of the piezotronics based on *a*-axis nano/microwires. (a) The principle of the piezoelectric field-effect transistor (PE-FET). (b) The principle of the piezoelectric gated diode [29] John Wiley & Sons. [© 2007 WILEY-VCH Verlag GmbH & Co. KGaA, Weinheim]. (c)–(e) Schematic illustration of the working mechanism of GaN nanobelt SGTs (c) under strain free condition; (d) as applying −0.5% compressive strains at the initial stage; (e) under −0.5% compressive strains at equilibrium. Top panels: FEA simulations of piezoelectric potential distributions; bottom panels: schematic illustration of carriers' motions. (c)–(e) Reprinted with permission from [46]. Copyright (2015) American Chemical Society.

different tensile/compressive strains is schematically illustrated in figures 4(c)–(e) [46]. The finite element method (FEM) is utilized to calculate the piezoelectric potential (piezo-potential) distribution and the corresponding charge carriers' motion are depicted, as shown in the top and bottom panels, respectively. Under strain free condition, no piezo-potential is produced inside the GaN nanobelt, and therefore the majority carriers electrons are distributed uniformly in the whole GaN nanobelt as an n-type semiconductor material (figure 4(c)). At the initial stage of applying a compressive strain of −0.5% along the *a*-axis direction, an instantaneous piezo-potential distribution is produced, with positive and negative piezoelectric polarization charges (piezo-charges) located at top and bottom surface of the nanobelt, respectively (figure 4(d), top panel). As a result, the electrons are attracted by the positive piezo-charges and repelled by the negative piezo-charges, forming a motion of moving upward of the electrons (figure 4(d), bottom panel). When the equilibrium is achieved, as illustrated in the bottom panel of figure 4(e), electrons are accumulated at the top region of the nanobelt and screen the positive piezo-charges, whereas a depletion region is formed at the bottom of the nanobelt [47], which agrees well with the calculated piezo-potential distribution presented in the top panel of figure 4(e). For the tensile strain condition, similar charge carrier and piezo-potential distributions are expected, with electrons accumulating and screening the positive piezo-charges at the bottom region, and the depletion region being formed at the top region, correspondingly. Consequently, the charge carriers' transportation properties can be effectively modulated by externally applied tensile/compressive strains *via* forming a depletion region to shrink the conduction channel width and hence increase the resistance of the nanobelt. This is the volumetric effects of piezotronics in *a*-axis piezoelectric semiconductor materials. In addition, when two metal electrodes are deposited at both ends of the nanobelt with two Schottky contacts formed as the drain and source terminals, the SBHs of both Schottky junctions will be increased as the negative piezo-charges are presented due to the screening of positive piezo-charges by the majority electrons inside the nanobelt. The increase of SBHs at the two metal/GaN nanobelt contacts will then result in the hindering of the electrons' transport across the locate metal–semiconductor interfaces, which is equivalent to the resistance increase of the metal–semiconductor–metal device. This is the interface effects of piezotronics in *a*-axis piezoelectric semiconductor materials. Therefore, the *a*-axis piezotronics are mainly based on both the volumetric and interfacial effects.

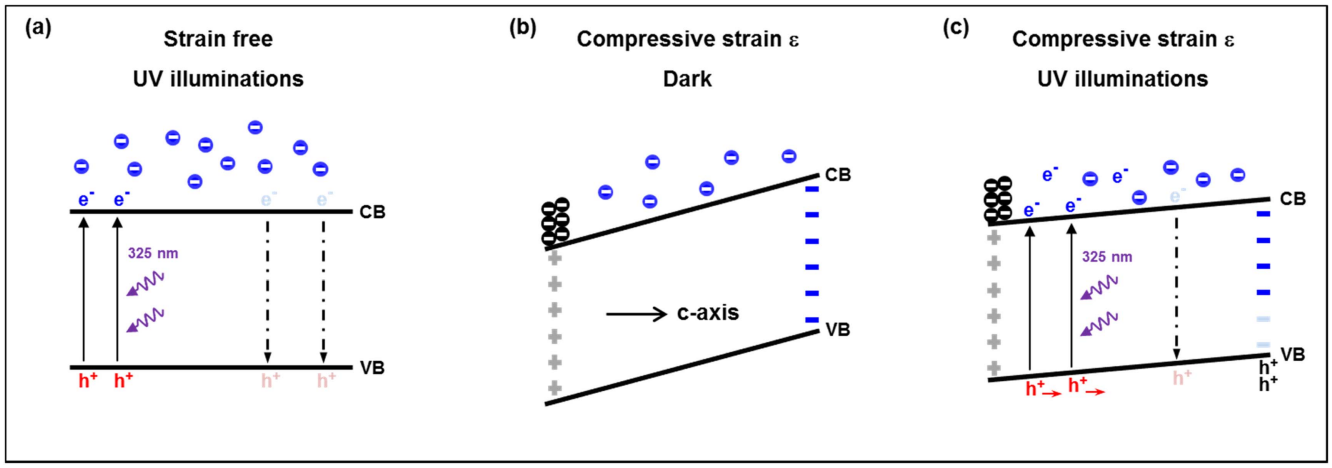

Figure 5. At room temperature, the energy band diagram under (a1) strain free condition, (b1) and (c1) compressive strains along the *c*-axis (b1) in the dark, and (c1) under UV illumination. [48] John Wiley & Sons. [© 2015 WILEY-VCH Verlag GmbH & Co. KGaA, Weinheim].

Figure 5 is a room temperature energy band diagram along *c*-axis direction of the *a*-axis nanobelt under strain free and compressive strain (along *c*-axis, i.e. tensile strain along *a*-axis) conditions for illustrating the piezophototronics in *a*-axis piezoelectric semiconductor materials [48]. Normally, both the photo-generation and recombination of electron–hole pairs occur when the nanobelt is illuminated with UV laser (figure 5(a)). After the compressive strain along *c*-axis is applied, the produced positive and negative piezo-potentials will tilt the energy band (figure 5(b)). Upon UV illumination, the photo-generated holes are readily attracted and trapped by the unscreened negative piezo-potential, leaving the photo-generated electrons alone (figure 5(c)). These unpaired photo-generated electrons are then drifted along the *a*-axis direction under bias voltage and collected by the electrodes, contributing to the photocurrent. With the increase of externally applied compressive strain along *c*-axis, the negative piezo-potential increases and thus is able to attract more photo-generated holes, leaving more unpaired photo-generated electrons for the contribution of photocurrent. Similar modulations of the separation and collection of the photo-generated electron–hole pairs are expected when tensile strains are applied along *c*-axis direction. Therefore, these results indicate that the piezophototronics in *a*-axis piezoelectric semiconductor materials is mainly a volumetric effect, different from that observed in *c*-axis piezoelectric semiconductor materials.

4.3. Temperature dependence of the piezotronic and piezophototronic effect in a-axis GaN microwire

The piezo-potential distribution of the *a*-axis GaN nanobelt under 0.28% tensile strain and at 77 K are simulated through the FEM [48] and the overall and cross-sectional views are presented in figure 6(a). As analyzed before, the positive piezo-potential will attract the electrons and be screened by the accumulated electrons, producing a depletion region at the negative piezo-potential side. When the temperature decreases from room temperature (300 K) to low temperature (77 K), it is expected that the mobile free electrons are decreased due to the freeze-out effect [49], in turn reducing the screening of positive piezo-potential. As a result, more electrons are attracted by the increased effective positive piezo-potential, leading to the increase of the depletion region width. The depletion region width and corresponding relative change of the width under 0.28% tensile strain at different temperatures from 300 to 77 K are then calculated and summarized in figure 6(b), obviously indicating the increase of the depletion region width and the strengthen of the piezotronics in *a*-axis piezoelectric semiconductor materials as decreasing the temperature.

For the piezophototronics at low temperature, it is schematically illustrated in figures 6(c)–(e), with low temperature energy band diagram along *c*-axis direction of the *a*-axis nanobelt under strain free and compressive strain (along *c*-axis, i.e. tensile strain along *a*-axis) conditions. Due to the freeze-out effect, part of the free electrons are trapped in the shallow impurity centers with activation energy of about 20–30 meV [50, 51], which can be easily activated by the incident UV photons. Consequently, the photocurrent at low temperature consists of both the band gap excitation and the activation of trapped electrons, while only band gap excitation contributes to the photocurrent at room temperature (figure 6(c)). When compressive strain along *c*-axis direction is applied (figure 6(d)), more effective positive and negative piezo-potentials are produced due to the reduced screening effects of decreased free electrons, leading to a more drastic tilting of the energy band diagram. Upon UV illumination (figure 6(e)), on one hand, the photo-generated electrons could be attracted and trapped by the increased effective positive piezo-potential, which would decrease the photocurrent; on the other hand, the tilted energy band diagram makes the impurity centers closer to the conduction band, which would facilitate the activation of trapped electrons and thus increase the photocurrent. These two processes compete with each other, and as a result, at low temperature the photocurrent is expected to represent a local extreme as increasing the compressive strain along *c*-axis direction, while at

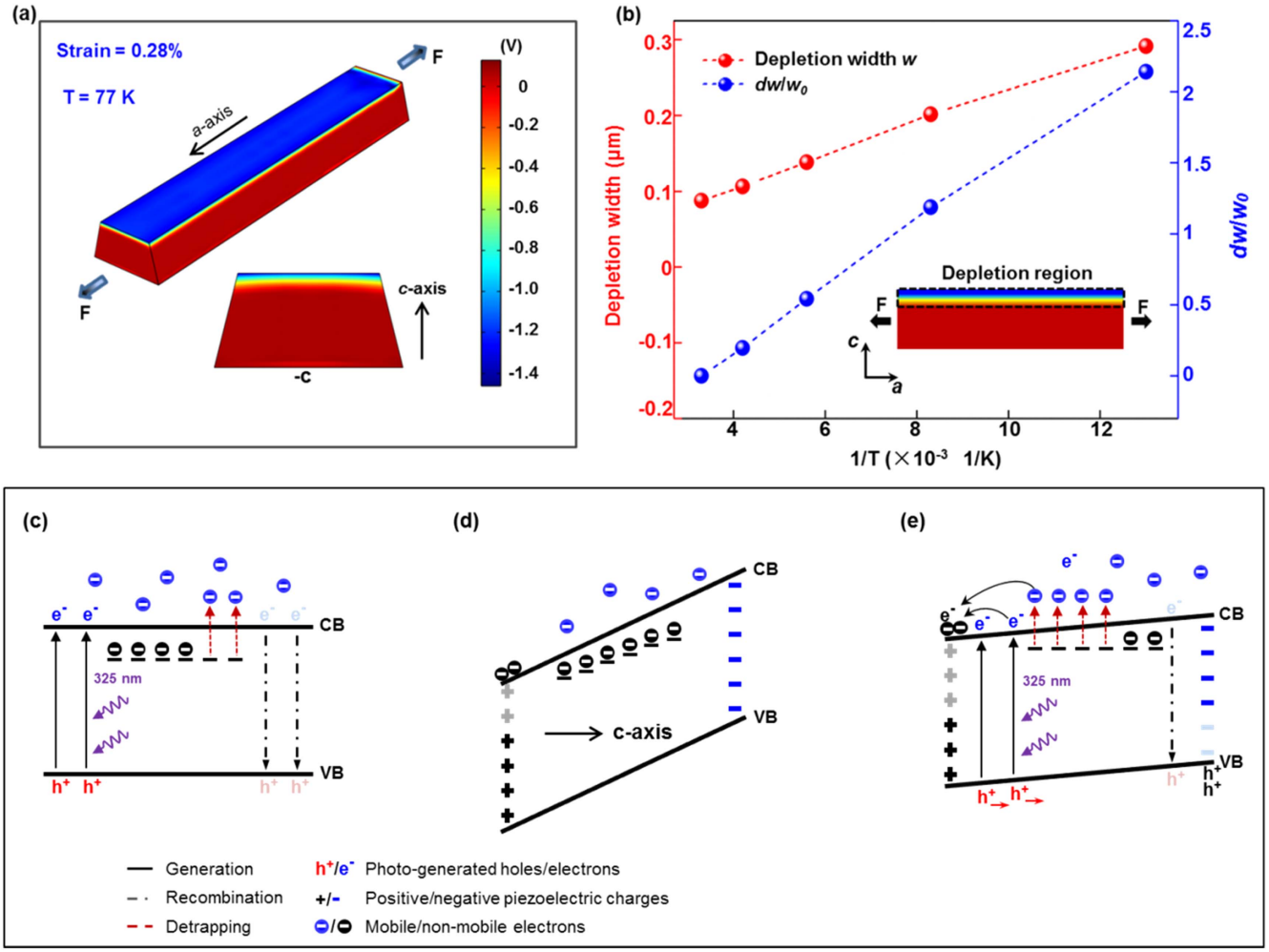

Figure 6. Working mechanisms of temperature dependence of the piezo-phototronic effect. At room temperature, the energy band diagram under (a1) strain free condition, (b1) and (c1) compressive strains along the *c*-axis (b1) in the dark, and (c1) under UV illumination. At low temperature, the energy band diagram under (a2) strain free condition, (b2) and (c2) compressive strains along the *c*-axis (b2) in the dark, and (c2) under UV illumination. [48] John Wiley & Sons. [© 2015 WILEY-VCH Verlag GmbH & Co. KGaA, Weinheim].

room temperature the photocurrent increases monotonously with the compressive strain along *c*-axis direction.

5. Applications

5.1. Piezotronic gated a-axis GaN transistor

By applying silver paste at both ends of the *a*-axis GaN nanobelt to form two Schottky contacts, a piezotronic gated *a*-axis GaN transistor is demonstrated [46]. The morphology of the as-synthesized GaN nanobelt characterized by scanning electron microscopy (SEM) clearly shows a trapezoidal cross section as the inset with height of 1 μm, width of 2 μm and length of 100–200 μm, as presented in figure 7(a). High resolution transmission electron microscopy (HRTEM) (figures 7(b1) and (b3)) and corresponding selected area electron diffraction (SAED) patterns (figures 7(b2) and (b4)) are utilized to confirm that the *a*-axis is along the length direction of the GaN nanobelt. Then, by sweeping the bias from -3 to $+3$ V and applying different tensile/compressive strains, the piezotronic effect on the current–voltage (I–V) characteristics of the *a*-axis GaN nanobelt is studied systematically. Clearly from the results as shown in figures 7(c) and (d), the output current decreases as increasing the tensile or the compressive strains. The as-derived pseudo-transconductance g_m shown in the insets indicates the effective gating behavior of the *a*-axis GaN transistor by the externally applied strains. The current and corresponding resistance changes at bias of $+3$ V are then calculated and plotted in figure 7(e), indicating the symmetric changes of current/resistance, which is totally distinguishable from the asymmetric changes of current/resistance observed in *c*-axis piezotronic gated transistors.

5.2. Piezo-phototronic enhanced photoresponse of a-axis GaN UV photosensor

The back-to-back double Schottky junctions based *a*-axis GaN nanobelt transistor's UV sensing performance to 325 nm

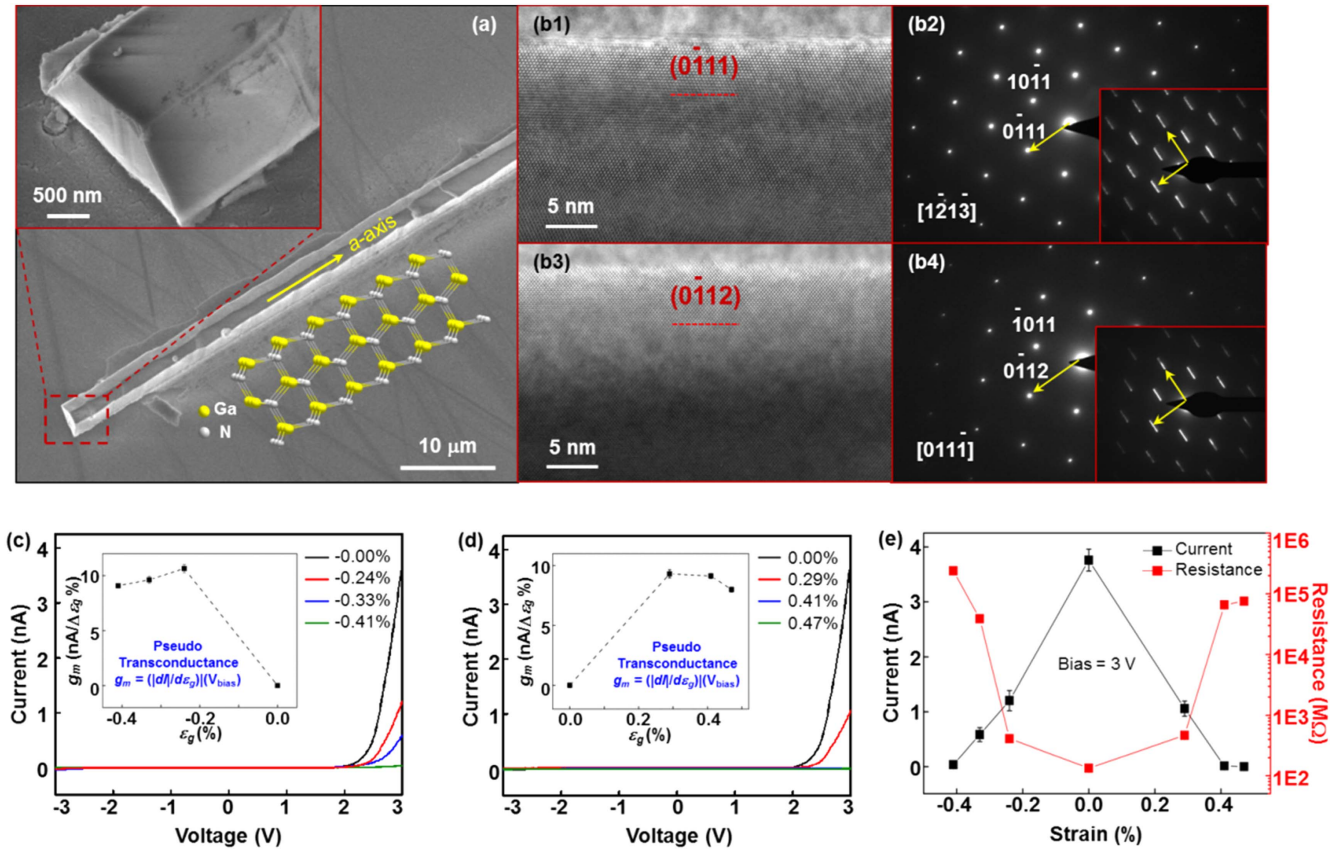

Figure 7. Characteristics of *a*-axis GaN nanowire and performances of piezotronic-gated transitor (a) SEM images of the as-synthesized GaN nanobelt with trapezoidal cross section as the inset. (b) HRTEM images (b1), (b3) and the corresponding SAED patterns (b2), (b4) of GaN nanobelts. (c) and (d) *I–V* characteristics of GaN nanobelt SGTs under a series of (a) compressive and (b) tensile strains under triangular wave ranging from –3 to +3 V. The insets are the corresponding pseudo-transconductance at 3 V. (e) Current and resistance response to strains at a bias voltage of 3 V. Reproduced with permission [46]. Copyright (2015) American Chemical Society.

UV laser under different temperatures are also investigated [48]. The SEM, HRTEM, and SAED techniques are utilized to further confirm the *a*-axis of the as-synthesized GaN nanobelt, as shown in figure 8(a). Figure 8(b) sketches the low temperature experimental set-up, indicating that one end of the as-fabricated device is fixed at the edge of the sample mount while the other end is manipulated by a probe for introduction of the strains. The whole system is set in a vacuum chamber and can be cooled down to 77 K by using liquid nitrogen. The UV laser can be guided and illuminated on the device through the quartz window at the top of the whole system. The photocurrent of the device under different strains and temperatures are measured, calculated and summarized in figure 8(c). At room temperature, the photocurrent increases monotonously and significantly as increasing the tensile strain along *a*-axis direction. However, the photocurrent first decreases and then increases with the tensile strain along *a*-axis direction at low temperature, which is caused by the two competing processes occurred due to the low temperature piezophototronic effect. Figure 8(d) is the derived gauge factor for evaluating the strain's modulation of the UV sensing performance at different temperatures. Clearly, the piezophototronic effect induced photocurrent enhancement of *a*-axis GaN nanobelt reaches maximum at room temperature and it decreases gradually as the temperature decreases, due to the two competing processes only presented at low temperatures.

5.3. Piezotronic modulated heterojunction electron gas (HEG) in AlGaN/GaN heterostructured microwire

1D semiconductor NWs have been extensively studied for various functional applications such as light emitting diode [52, 53], laser [54, 55], field-effect transistor [56, 57] and nanogenerator [26, 58, 59] due to their large surface-to-volume ratio and superior electric transport properties to outperform their planar counterparts. However, the carrier mobility degradation, resulted from scatterings of lattice vibration and/or charged dopant centers, has long been an inevitable obstacle for performances improvement of devices incorporating doped NWs for practical applications. To address these issues, heterostructure electron or hole gas formed and observed at the interface of semiconductor heterostructure, such as Ge/Si [60, 61], AlGaAs/GaAs [62] and AlGaN/GaN [63] have attracted considerable interests for applications in novel functional electronics. A potential well is formed at local heterojunctions by the band structure engineering induced by the spontaneous polarization and intrinsic piezoelectric polarization caused by lattice mismatch. This potential well can serve as a carrier transport channel that

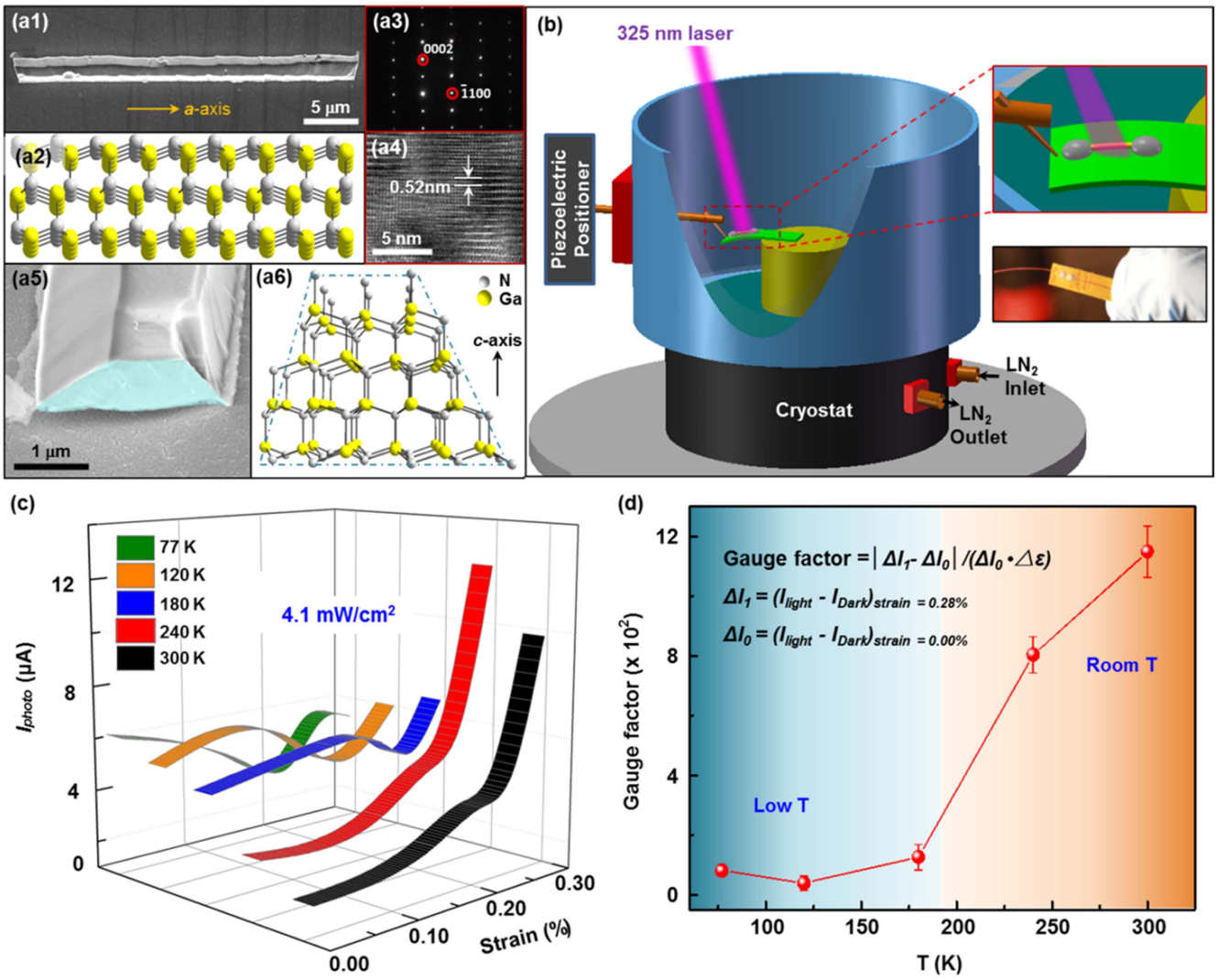

Figure 8. Nanowire structure, experimental setup and device performances (a1) SEM image and (a2) the corresponding atomic model of the GaN NB synthesized along *a*-axis. (a3) SAED pattern, (a4) HRTEM image, (a5) SEM image and (a6) the corresponding atomic model of the cross section of the *a*-axis GaN NB. (b) Schematic illustration of the experimental set-up and the digital image of a real device. (c) Under the illumination identity of 4.1 mW cm^{-2}, the photocurrent ($I_{photo} = I_{light} - I_{dark}$) *versus* tensile strains at various temperatures. (d) Photocurrent gauge factor as a function of system temperature. [48] John Wiley & Sons. [© 2015 WILEY-VCH Verlag GmbH & Co. KGaA, Weinheim].

is spatially separated from the ion doping region, and thus the impurity scattering of the charge carriers is significantly reduced/eliminated with substantially enhanced mobility. Among the semiconductor heterostructures mentioned above, AlGaN/GaN is one of the most ideal and suitable III-nitride material systems for creating superior-mobility HEG due to the strong intrinsic polarizations within GaN and AlGaN [64], and has been widely explored for high electron mobility transistor (HEMTs) and other high-performances quantum electronics [65]. According to the previous studies, tuning the growth parameters (Al mole compositions and/or thickness) is the most effective approach to control the physical properties of the induce HEG and thus engineering and optimizing devices performances [66–70]. Nevertheless, this method will increase the fabrication complexity and add additional expenses of the devices, which hinder the further improvement of their practical applications. Therefore, it is of great significance to develop novel, easier and more effective approaches to modulate the HEG in HEMTs.

The AlGaN/AlN/GaN heterostructured microwire (MW) for generation of the HEG is synthesized by metal organic chemical vapor deposition on patterned silicon substrate [71], as illustrated in figure 9(a). After the growth of *a*-axis GaN microwire, AlN and AlGaN are then deposited on the GaN microwire sequentially to form the AlGaN/AlN/GaN heterostructure. Figure 9(b) is the cross-section high-angle annular dark-field scanning transmission electron microscopy (HAADF–STEM) image of AlGaN/AlN/GaN heterostructure microwire, indicating a trapezoidal cross section with top width of ~100 nm, bottom width of ~1.5 μm and height of ~1.5 μm. The SAED pattern and lattice-resolved HAADF–STEM image (figure 9(c)) confirm that the microwire's length is along the non-polar *a*-axis direction, with its polar *c*-axis direction pointing to its top surface. Based on the image shown in figure 9(c), the atomic structure model and

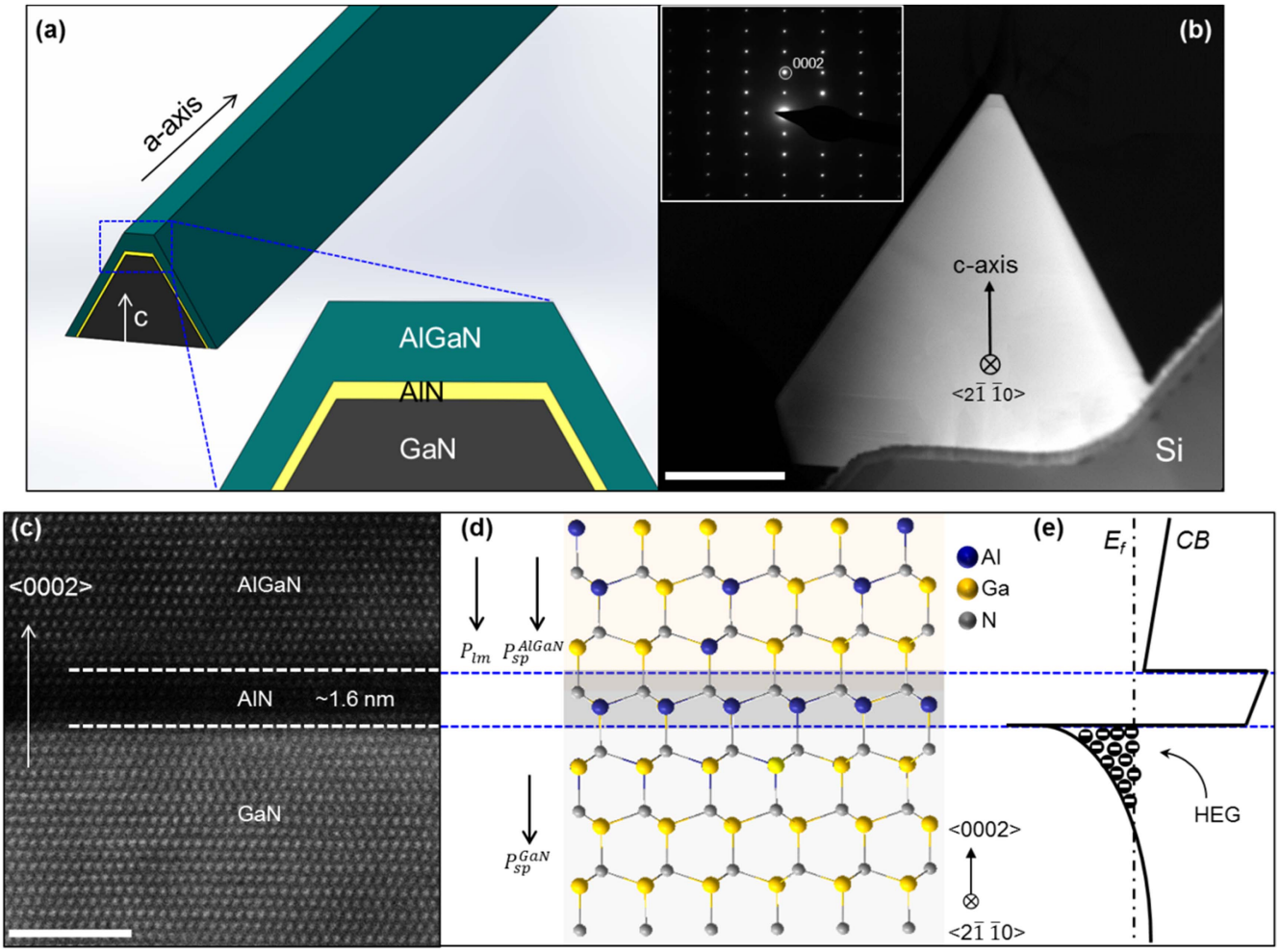

Figure 9. Structure characteristics of the heterostructure microwire. (a) Schematic diagram of an individual heterostructure microwire and magnified cross-sectional view of a microwire facet highlighting AlGaN/AlN/GaN structure. (b) The cross-section HAADF–STEM image of an individual AlGaN/AlN/GaN heterostructure microwire. The scale bar is 500 nm. Inset: corresponding electron diffraction pattern. (c) The lattice-resolved HAADF–STEM image of the interfacial region of AlGaN/AlN/GaN heterostructure. (d) Corresponding atomic structure model. (e) Corresponding conduction band profile and the distribution of HEG. [71] John Wiley & Sons. [© 2016 WILEY-VCH Verlag GmbH & Co. KGaA, Weinheim].

conduction band profile of the AlGaN/AlN/GaN heterostructure are obtained in figures 9(d) and (e). Two different types of naturally existed polarizations are presented in the AlGaN/AlN/GaN heterostructure, including the spontaneous polarization in AlGaN and GaN, and the lattice-mismatch-induced piezoelectric polarizations in AlGaN [72–74]. As a result, net positive fixed charges are accumulated at AlGaN/AlN/GaN interface. Moreover, a triangle-shaped quantum potential well is formed in GaN near the AlN/GaN interface, since the conduction band of GaN lies below that of AlGaN. In this manner, electrons are attracted, accumulated, and confined in this potential well and therefore the HEG is formed.

By transferring a single AlGaN/AlN/GaN microwire to the flexible polyester substrate and then depositing two ITO electrodes to form the Ohmic contacts at both ends of the microwire, a device for characterizing the strain effect on the HEG is prepared. One end of the device is fixed and the other end can be manipulated by a 3D stage to apply tensile/compressive strains, as shown in figure 10(a). The *I*–*V* characteristics of the device under different tensile/compressive strains are plotted in figure 10(b), clearly showing that the current increases with the compressive strain and decreases with the tensile strain. Then the conductance *G* and its relative change under different tensile/compressive strains are calculated and summarized in figure 10(c), indicating effective modulation of the conductance as well as the concentration of HEG of AlGaN/AlN/GaN heterostructure by externally applied strains. By calculating the fixed polarization charges distributed at the bottom surface of AlGaN and the absolute value of the fixed polarization charges distributed at the top surface of GaN as a function of the externally applied strains (figure 10(d)), the effective net fixed polarization charges σ^{int} of the AlGaN/AlN/GaN heterostructure can be derived at different strains, as shown in figure 10(e). It is noteworthy that the σ^{int} is positive under all the strain conditions and increases/decreases with the compressive/tensile strains, which agrees well with the experimental results and shows the modulation behavior by externally applied strains.

To study the underlying physical mechanism of the piezotronic effect on the modulation of HEG in AlGaN/AlN/

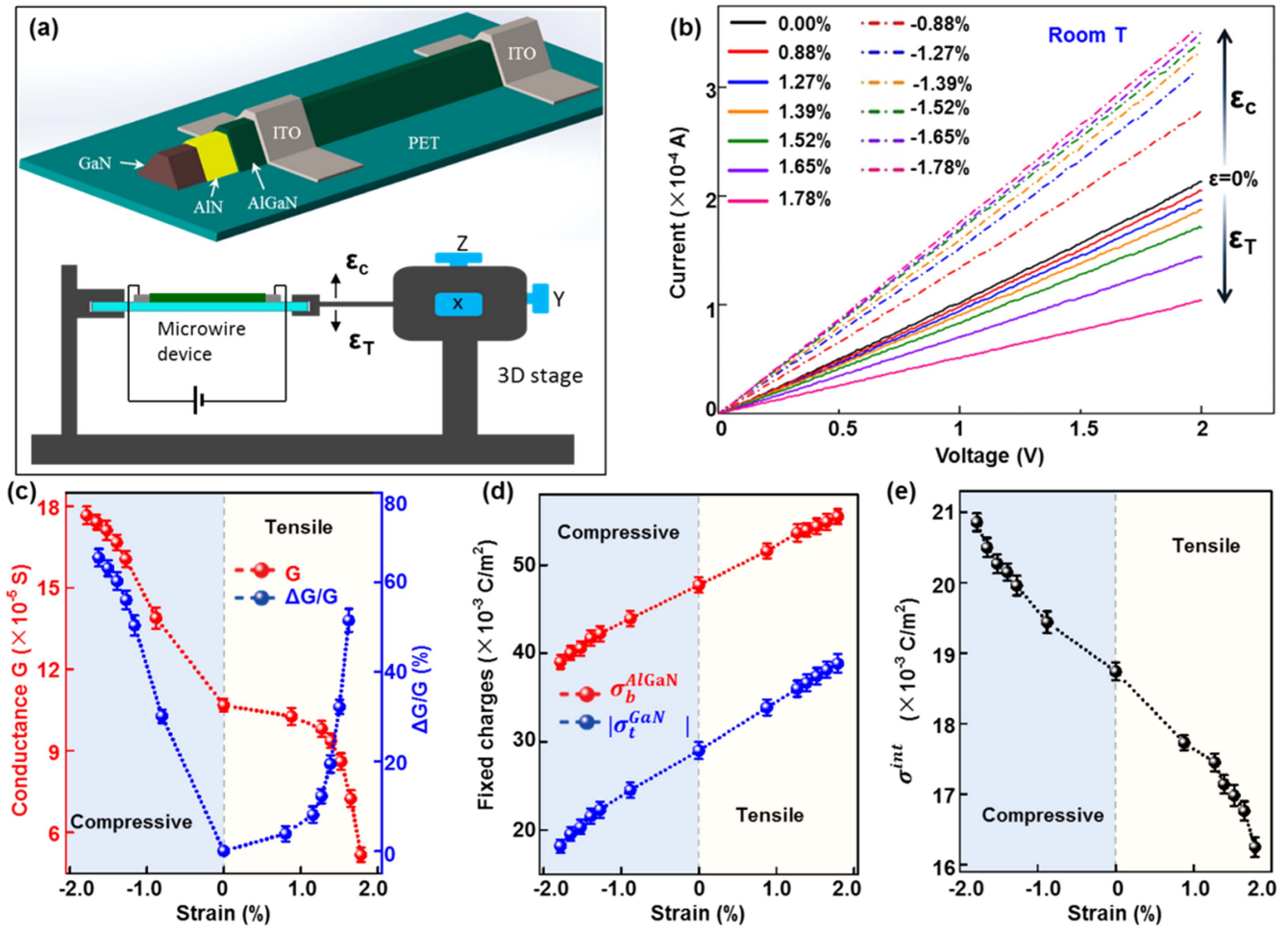

Figure 10. Piezotronic-effect-induced modulation of the heterostructure microwire. (a) Experimental set-ups (lower) and the schematics (upper) of the microwire devices. (b) *I–V* characteristics of the as-fabricated microwire devices under strain free and a series of compressive and tensile strains condition. (c) The conductance (G) and the corresponding relative changes ($\Delta G/G$) of the microwire devices as a function of strains. (d) The fixed polarization charges distributed at the bottom surface of AlGaN layer (σ_b^{AlGaN}) and the absolute value of fixed polarization charges distributed at the top surface of GaN ($|\sigma_t^{GaN}|$) as a function of applied external strains. (e) The effective net fixed polarization charges (σ^{int}) at AlGaN/AlN/GaN heterojunctions as a function of externally applied strains. [71] John Wiley & Sons. [© 2016 WILEY-VCH Verlag GmbH & Co. KGaA, Weinheim].

GaN heterostructure, self-consistent numerical calculations are conducted to calculate the energy band diagrams along the c-axis of AlGaN/AlN/GaN heterostructure under different compressive and tensile strain conditions [75–78]. The calculated conduction band of the AlGaN/AlN/GaN heterostructure and corresponding sheet density of HEG under strain free condition are shown in figure 11(a), suggesting that an deep potential well is induced in GaN side close to local AlN/GaN interface and the HEG with high sheet density is formed and distributed within this potential well. For the tensile strain condition, it is totally different. Upon tensile strain along the a-axis direction is applied, negative and positive piezo-charges are generated at the +c and −c planes, respectively, decreasing the conduction band at the AlGaN/AlN interface whereas increasing the conduction band at the AlN/GaN interface, as shown in figure 11(b)–(d). As a result, the concentration of the HEG is decreased, since the potential well becomes 'shallower' and the corresponding electron confinement is reduced. Furthermore, the σ^{int} also decreases with tensile strain, releasing a certain amount of the attracted and confined electrons.

When the compressive strain along the a-axis direction is applied (figure 12), positive and negative piezo-charges are produced at the $+c$ and $-c$ planes, respectively, increasing the conduction band at the AlGaN/AlN interface whereas decreasing the conduction band at the AlN/GaN interface, as shown in figures 12(a)–(c). The concentration of the HEG is therefore increased due to the potential well becoming 'deeper' and being able to attract and confine more electrons (figure 12(d)). Besides, the σ^{int} also increases with compressive strain, which also contribute to the attraction and accumulation of electrons into the potential well, as well as the concentration of HEG. The calculated peak concentration of the HEG of AlGaN/AlN/GaN heterostructure under different compressive and tensile strains are derived and plotted in figure 12(e), agreeing very well with the experimental results and presenting obvious effective modulation of the HEG *via* the piezotronic effect.

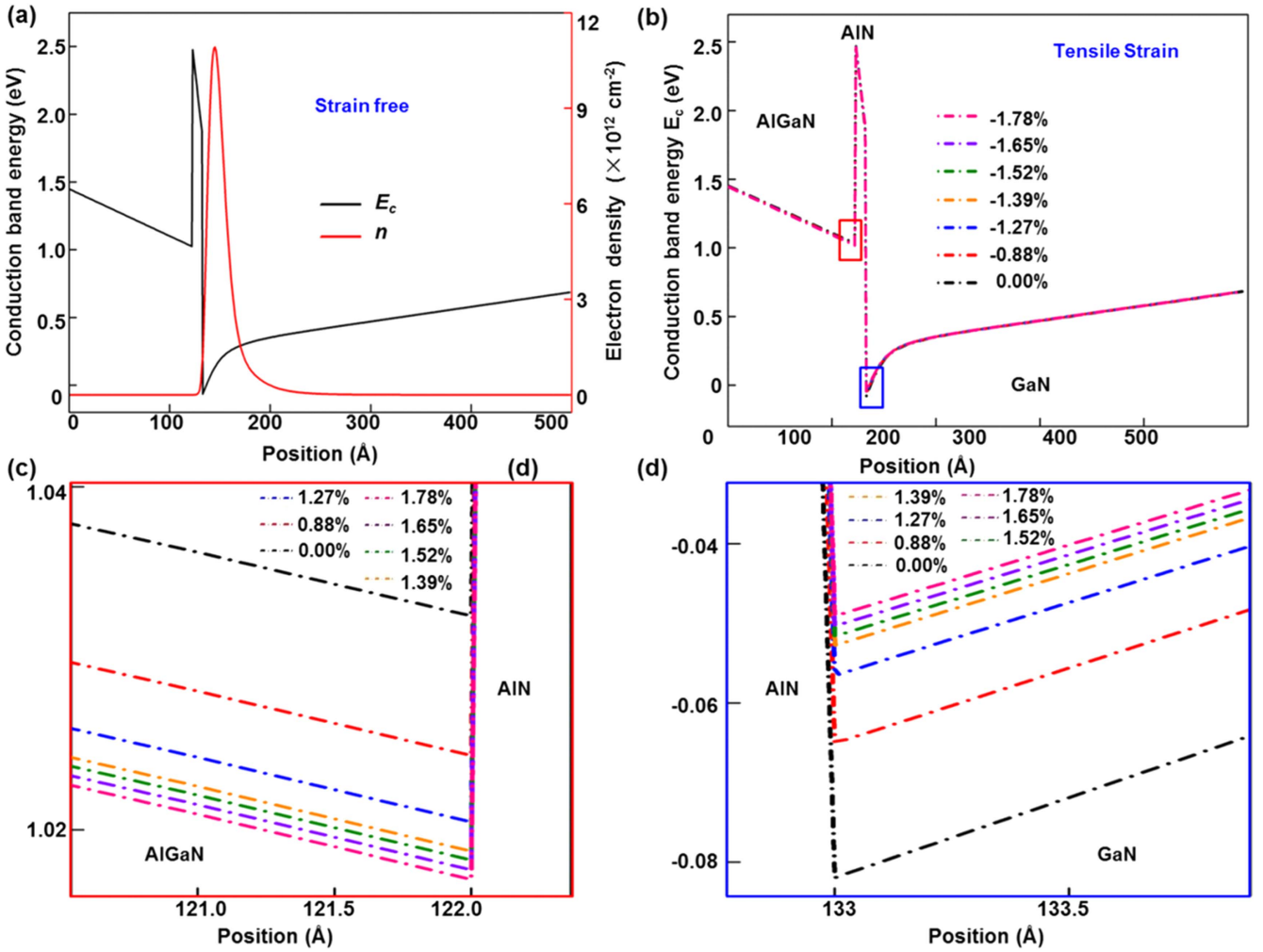

Figure 11. Theoretical calculation results under tensile strains. (a) The calculated conduction band of the AlGaN/GaN/GaN heterostructure and corresponding sheet density of HEG under strain free condition. (b) The conduction band energy profiles under strain free and tensile strains along *a*-axis of the heterostructure microwire. (c) The enlarged E_c of AlGaN/AlN heterojunction as labled by red rectangular box in (b). (d) The enlarged E_c of AlN/GaN heterojunction as labled by blue rectangular box in (b). [71] John Wiley & Sons. [© 2016 WILEY-VCH Verlag GmbH & Co. KGaA, Weinheim].

Different from other reported strategies such as modifying the alloy components or controlling the layer(s) thickness to adjust the HEG characteristics, the strain-induced piezocharges are utilized to modify the energy band profile at local heterojunctions as an effective way for physical properties control of HEG. This study provides in-depth understanding about the piezotronic-effect modulation of low-dimensional electron gas in heterostructured nanomaterials, and opens possible opportunity for potential applications in HEMTs and MEMS/NEMS.

6. Summary and perspectives

Piezotronics and piezo-phototronics are emerging fields involving the modulation and manipulation of the distribution and dynamics of the free charge carriers at local contact/junction by external applied strain for functional applications. The corresponding physical mechanisms of the piezotronic and piezo-phototronic effect rely on the coupling between strain-induced polarization and semiconductor properties in piezoelectric semiconductor materials. The presence of localized piezoelectric polarization charges can significantly modulate/control the charge carrier generation, separation, transport and/or recombination at an interface/junction in electric and optoelectronic processes.

Owing to the growth of 1D semiconductor nanostructure being preferentially along the polar ⟨0001⟩ direction, most of the previously reported piezotronic and piezo-phototronic devices are based on *c*-axis nano/microwires. The corresponding piezocharges are presented at the vicinity of the local interface at both ends of the polar-axis nano/microwires, which are utilized to modulate the potential barrier characteristics and energy band profile at the junction region, such as M–S junction and homo-/hetero-junction. However, the optical absorptions of these devices are relative weak due to the small effective junction area, which may hinder the performance improvement and practical applications of piezotronic/piezo-phototronic devices. In a non-polar *a*-axis nano/microwires, the external-strain-induced piezocharges are distributed along the whole polar surfaces, with the

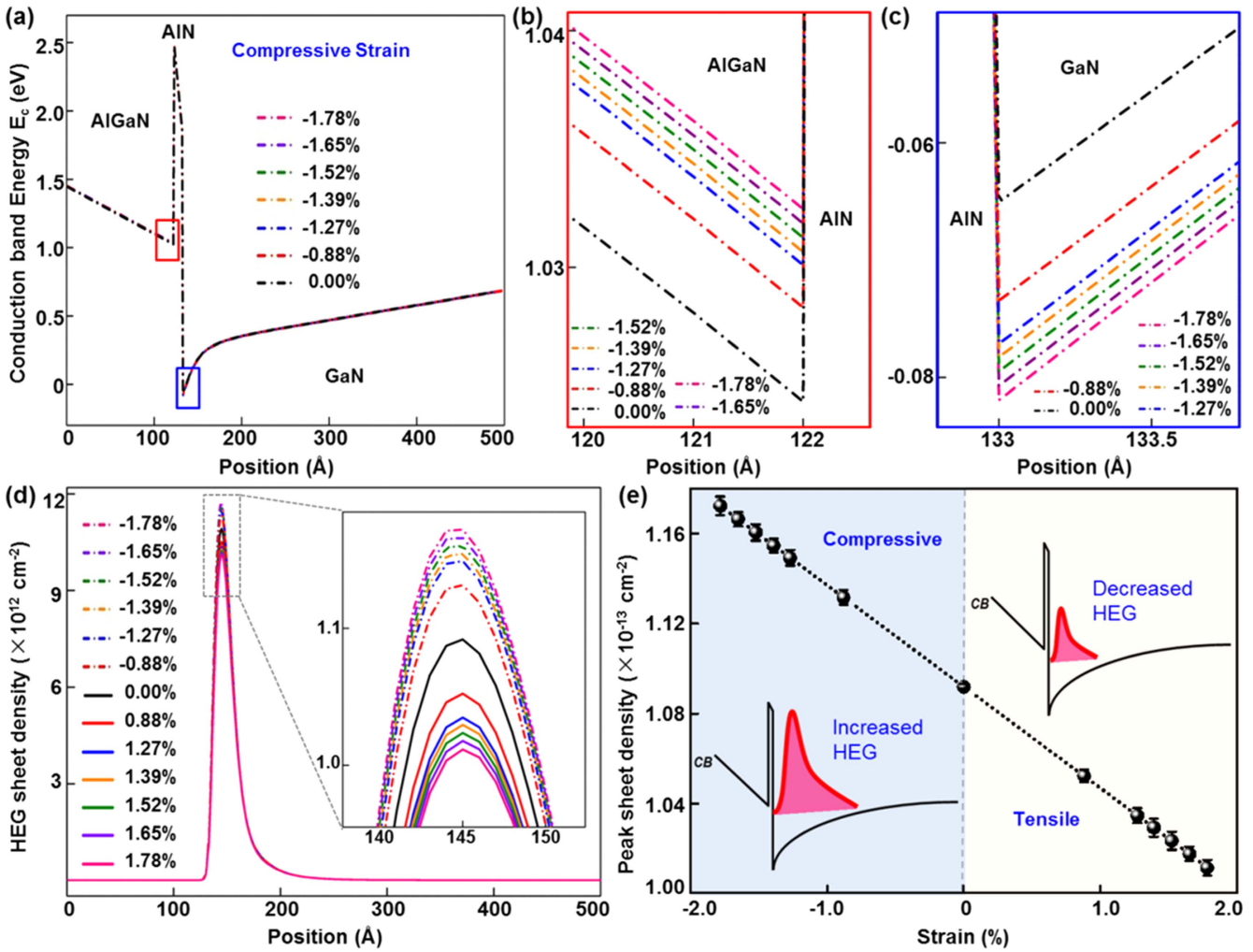

Figure 12. Theoretical calculation results under compressive strains. (a) The conduction band energy profiles under strain free and compressive strains along *a*-axis of the heterostructure microwire. (b) The enlarged E_c at AlGaN/AlN heterojunction as labeled by red rectangular box in (a). (c) The enlarged E_c at AlN/GaN heterojunction as labeled by blue rectangular box in (a). (d) The sheet density of HEG confined in the potential well under strain free, compressive and tensile strains condition. (e) Corresponding peak values of HEG sheet density extracted from (d). [71] John Wiley & Sons. [© 2016 WILEY-VCH Verlag GmbH & Co. KGaA, Weinheim].

direction across the width of the nano/microwire. The charge carriers transport processes of piezoelectric semiconductors are modulated by the piezotronic/piezo-phototronic effects within the entire body of the nanostructure. Fundamental research of piezotronics and piezo-phototronics based on *a*-axis nano/microwires as well as typical applications in this review introduce new concepts and understanding about the piezotronic and piezo-phototronic effects, which improve the fundamental theoretical framework of the piezotronics and piezophototronic. These demonstrations also provide guidance for the developments of novel high-performances piezotronic/piezo-phototronic devices by designing core–shell and radial heterostructure nanowire, such as intelligent human–electronics interfacing, high-speed electronics and high-efficiency light sources.

Acknowledgements

The authors thank the support from US Department of Energy, Office of Basic Energy Sciences (Award DE-FG02-07ER46394), and the 'thousands talents' program for pioneer researcher and his innovation team, China. We sincerely thank the following colleagues who made significant contributions to the work presented here: (not in any particular order): Dr Ruomeng Yu, Dr Weiguo Hu, Chunyan Jiang, Dr Wenzhuo Wu, Dr Yong Ding, Dr Shuti Li, Dr Yunlong Zi, Changsheng Wu and many others.

References

[1] Gerhardmulthaupt R 1985 Origin of the piezoelectricity in polyvinylidenefluoride *NTZ Arch.* **7** 133–43
[2] Sessler G M 1981 Piezoelectricity in polyvinylidenefluoride *J. Acoust. Soc. Am.* **70** 1596–608
[3] Yamada T, Ueda T and Kitayama T 1982 Piezoelectricity of a high-content lead zirconate titanate polymer composite *J. Appl. Phys.* **53** 4328–32
[4] Tzou H S and Tseng C I 1990 Distributed piezoelectric sensor actuator design for dynamic measurement control of distributed parameter-systems—a piezoelectric finite-element approach *J. Sound Vib.* **138** 17–34

[5] Giurgiutiu V 2005 Tuned lamb wave excitation and detection with piezoelectric wafer active sensors for structural health monitoring *J. Intell. Mater. Syst. Struct.* **16** 291–305

[6] Ikuta K, Kawahara A and Yamazumi S 1991 Miniature cybernetic actuators using piezoelectric device *Proc. IEEE Micro Electro Mechanical Systems (MEMS '91)* 131–6

[7] Crawley E F and Deluis J 1987 Use of piezoelectric actuators as elements of intelligent structures *AIAA J.* **25** 1373–85

[8] Gross S J, Tadigadapa S, Jackson T N, Trolier-McKinstry S and Zhang Q Q 2003 Lead–zirconate–titanate-based piezoelectric micromachined switch *Appl. Phys. Lett.* **83** 174–6

[9] Cueff M *et al* 2010 A fully packaged piezoelectric switch with low-voltage actuation and electrostatic hold *Proc. IEEE Micro Elecro* pp 212–5

[10] Renaud M, Karakaya K, Sterken T, Fiorini P, Van Hoof C and Puers R 2008 Fabrication, modelling and characterization of MEMS piezoelectric vibration harvesters *Sensors Actuators* A **145** 380–6

[11] Fang H B, Liu J Q, Xu Z Y, Dong L, Wang L, Chen D, Cai B C and Liu Y 2006 Fabrication and performance of MEMS-based piezoelectric power generator for vibration energy harvesting *Microelectron. J.* **37** 1280–4

[12] Ottman G K, Hofmann H F, Bhatt A C and Lesieutre G A 2002 Adaptive piezoelectric energy harvesting circuit for wireless remote power supply *IEEE Trans. Power Electr.* **17** 669–76

[13] Tseng K K and Wang L 2004 Smart piezoelectric transducers for *in situ* health monitoring of concrete *Smart Mater. Struct.* **13** 1017–24

[14] Wang Z L 2012 Progress in piezotronics and piezo-phototronics *Adv. Mater.* **24** 4632–46

[15] Wang Z L 2010 Piezopotential gated nanowire devices: piezotronics and piezo-phototronics *Nano Today* **5** 540–52

[16] Wang Z L 2012 From nanogenerators to piezotronics—a decade-long study of ZnO nanostructures *MRS Bull.* **37** 814–27

[17] Yamabi S and Imai H 2002 Growth conditions for wurtzite zinc oxide films in aqueous solutions *J. Mater. Chem.* **12** 3773–8

[18] Wu W Z, Wei Y G and Wang Z L 2010 Strain-gated piezotronic logic nanodevices *Adv. Mater.* **22** 4711–5

[19] Yu R M, Wu W Z, Ding Y and Wang Z L 2013 GaN nanobelt-based strain-gated piezotronic logic devices and computation *ACS Nano* **7** 6403–9

[20] Niu S M, Hu Y F, Wen X N, Zhou Y S, Zhang F, Lin L, Wang S H and Wang Z L 2013 Enhanced performance of flexible ZnO nanowire based room-temperature oxygen sensors by piezotronic effect *Adv. Mater.* **25** 3701–6

[21] Yu R M, Pan C F and Wang Z L 2013 High performance of ZnO nanowire protein sensors enhanced by the piezotronic effect *Energ. Environ. Sci.* **6** 494–9

[22] Yang Q, Wang W H, Xu S and Wang Z L 2011 Enhancing light emission of ZnO microwire-based diodes by piezo-phototronic effect *Nano Lett.* **11** 4012–7

[23] Pan C F, Chen M X, Yu R M, Yang Q, Hu Y F, Zhang Y and Wang Z L 2016 Progress in piezo-phototronic-effect-enhanced light-emitting diodes and pressure imaging *Adv. Mater.* **28** 1535–52

[24] Pan C F, Niu S M, Ding Y, Dong L, Yu R M, Liu Y, Zhu G and Wang Z L 2012 Enhanced Cu_2S/CdS coaxial nanowire solar cells by piezo-phototronic effect *Nano Lett.* **12** 3302–7

[25] Wang Z L 2008 Towards self-powered nanosystems: from nanogenerators to nanopiezotronics *Adv. Funct. Mater.* **18** 3553–67

[26] Wang Z L and Song J H 2006 Piezoelectric nanogenerators based on zinc oxide nanowire arrays *Science* **312** 242–6

[27] Gao Z Y, Zhou J, Gu Y D, Fei P, Hao Y, Bao G and Wang Z L 2009 Effects of piezoelectric potential on the transport characteristics of metal–ZnO nanowire-metal field effect transistor *J. Appl. Phys.* **106** 113707

[28] Wang Z L 2012 *Piezotronics and Piezo-Phototronics* (Berlin: Springer)

[29] Wang Z L N 2007 Nanopiezotronics *Adv. Mater.* **19** 889–92

[30] Shi J, Starr M B and Wang X D 2012 Band structure engineering at heterojunction interfaces via the piezotronic effect *Adv. Mater.* **24** 4683–91

[31] Wang Z L and Wu W Z 2014 Piezotronics and piezo-phototronics: fundamentals and applications *Natl Sci. Rev.* **1** 62–90

[32] Wu W Z and Wang Z L 2011 Piezotronic nanowire-based resistive switches as programmable electromechanical memories *Nano Lett.* **11** 2779–85

[33] Pradel K C, Wu W Z, Zhou Y S, Wen X N, Ding Y and Wang Z L 2013 Piezotronic effect in solution-grown p-type ZnO nanowires and films *Nano Lett.* **13** 2647–53

[34] Pradel K C, Wu W Z, Ding Y and Wang Z L 2014 Solution-derived ZnO homojunction nanowire films on wearable substrates for energy conversion and self-powered gesture recognition *Nano Lett.* **14** 6897–905

[35] Lu S N, Qi J J, Gu Y S, Liu S, Xu Q K, Wang Z Z, Liang Q J and Zhang Y 2015 Influence of the carrier concentration on the piezotronic effect in a ZnO/Au Schottky junction *Nanoscale* **7** 4461–7

[36] Xue F, Zhang L M, Feng X L, Hu G F, Fan F R, Wen X N, Zheng L and Wang Z L 2015 Influence of external electric field on piezotronic effect in ZnO nanowires *Nano Res.* **8** 2390–9

[37] Lee K Y, Bae J, Kim S, Lee J H, Yoon G C, Gupta M K, Kim S, Kim H, Park J and Kim S W 2014 Depletion width engineering via surface modification for high performance semiconducting piezoelectric nanogenerators *Nano Energy* **8** 165–73

[38] Wang C H, Liao W S, Ku N J, Li Y C, Chen Y C, Tu L W and Liu C P 2014 Effects of free carriers on piezoelectric nanogenerators and piezotronic devices made of GaN nanowire arrays *Small* **10** 4718–25

[39] Sze S M and Ng K K 2006 *Physics of Semiconductor Devices* (New York: Wiley)

[40] He J H, Hsin C L, Liu J, Chen L J and Wang Z L 2007 Piezoelectric gated diode of a single ZnO nanowire *Adv. Mater.* **19** 781–5

[41] Wang Z L 2007 The new field of nanopiezotronics *Mater Today* **10** 20–8

[42] Wang Z L 2012 Preface to the special section on piezotronics *Adv. Mater.* **24** 4630–1

[43] Zhang Y and Wang Z L 2012 Theory of piezo-phototronics for light-emitting diodes *Adv. Mater.* **24** 4712–8

[44] Yu R M, Niu S M, Pan C F and Wang Z L 2015 Piezotronic effect enhanced performance of Schottky-contacted optical, gas, chemical and biological nanosensors *Nano Energy* **14** 312–39

[45] Wu W Z and Wang Z L 2016 Piezotronics and piezo-phototronics for adaptive electronics and optoelectronics *Nat. Rev. Mater* **1** 16031

[46] Yu R M, Wang X F, Peng W B, Wu W Z, Ding Y, Li S T and Wang Z L 2015 Piezotronic effect in strain-gated transistor of *a*-axis GaN nanobelt *ACS Nano* **9** 9822–9

[47] Gao Y and Wang Z L 2009 Equilibrium potential of free charge carriers in a bent piezoelectric semiconductive nanowire *Nano Lett.* **9** 1103–10

[48] Wang X F, Yu R M, Peng W B, Wu W Z, Li S T and Wang Z L 2015 Temperature dependence of the piezotronic and piezophototronic effects in *a*-axis gan nanobelts *Adv. Mater.* **27** 8067–74

[49] Slack G A, Schowalter L J, Morelli D and Freitas J A 2002 Some effects of oxygen impurities on AlN and GaN *J. Cryst. Growth* **246** 287–98

[50] Molnar R J, Lei T and Moustakas T D 1993 Electron-transport mechanism in gallium nitride *Appl. Phys. Lett.* **62** 72–4

[51] Moore W J, Freitas J A, Braga G C B, Molnar R J, Lee S K, Lee K Y and Song I J 2001 Identification of Si and O donors in hydride-vapor-phase epitaxial GaN *Appl. Phys. Lett.* **79** 2570–2

[52] Guo W, Zhang M, Banerjee A and Bhattacharya P 2010 Catalyst-free InGaN/GaN nanowire light emitting diodes grown on (001) silicon by molecular beam epitaxy *Nano Lett.* **10** 3355–9

[53] Qian F, Gradecak S, Li Y, Wen C Y and Lieber C M 2005 Core/multishell nanowire heterostructures as multicolor, high-efficiency light-emitting diodes *Nano Lett.* **5** 2287–91

[54] Huang M H, Mao S, Feick H, Yan H Q, Wu Y Y, Kind H, Weber E, Russo R and Yang P D 2001 Room-temperature ultraviolet nanowire nanolasers *Science* **292** 1897–9

[55] Qian F, Li Y, Gradecak S, Park H G, Dong Y J, Ding Y, Wang Z L and Lieber C M 2008 Multi-quantum-well nanowire heterostructures for wavelength-controlled lasers *Nat. Mater.* **7** 701–6

[56] Cui Y, Zhong Z H, Wang D L, Wang W U and Lieber C M 2003 High performance silicon nanowire field effect transistors *Nano Lett.* **3** 149–52

[57] Li Q L, Zhu X X, Yang Y, Ioannou D E, Xiong H D, Kwon D W, Suehle J S and Richter C A 2009 The large-scale integration of high-performance silicon nanowire field effect transistors *Nanotechnology* **20** 415202

[58] Chen C Y, Zhu G, Hu Y F, Yu J W, Song J H, Cheng K Y, Peng L H, Chou L J and Wang Z L 2012 Gallium nitride nanowire based nanogenerators and light-emitting diodes *ACS Nano* **6** 5687–92

[59] Qin Y, Wang X D and Wang Z L 2008 Microfibre-nanowire hybrid structure for energy scavenging *Nature* **451** 809–813

[60] Xiang J, Lu W, Hu Y J, Wu Y, Yan H and Lieber C M 2006 Ge/Si nanowire heterostructures as high-performance field-effect transistors *Nature* **441** 489–93

[61] Fukata N, Yu M, Jevasuwan W, Takei T, Bando Y, Wu W Z and Wang Z L 2015 Clear experimental demonstration of hole gas accumulation in Ge/Si core–shell nanowires *ACS Nano* **9** 12182–8

[62] Miao X and Li X L 2011 Scalable monolithically grown AlGaAs–GaAs planar nanowire high-electron-mobility transistor *IEEE Electron Device Lett.* **32** 1227–9

[63] Li Y, Xiang J, Qian F, Gradecak S, Wu Y, Yan H, Yan H, Blom D A and Lieber C M 2006 Dopant-free GaN/AlN/AlGaN radial nanowire heterostructures as high electron mobility transistors *Nano Lett.* **6** 1468–73

[64] Ambacher O *et al* 2000 Two dimensional electron gases induced by spontaneous and piezoelectric polarization in undoped and doped AlGaN/GaN heterostructures *J. Appl. Phys.* **87** 334–44

[65] Vandenbrouck S, Madjour K, Theron D, Dong Y J, Li Y, Lieber C M and Gaquiere C 2009 12 GHz F-MAX GaN/AlN/AlGaN nanowire MISFET *IEEE Electron Device Lett.* **0** 322–4

[66] Smorchkova I P, Chen L, Mates T, Shen L, Heikman S, Moran B, Keller S, DenBaars S P, Speck J S and Mishra U K 2002 AlN/GaN and (Al,Ga)N/AlN/GaN two-dimensional electron gas structures grown by plasma-assisted molecular-beam epitaxy *J. Appl. Phys.* **90** 5196

[67] Zhang Y F and Singh J 1999 Charge control and mobility studies for an AlGaN/GaN high electron mobility transistor *J. Appl. Phys.* **85** 587–94

[68] Smorchkova I P, Elsass C R, Ibbetson J P, Vetury R, Heying B, Fini P, Haus E, DenBaars S P, Speck J S and Mishra U K 1999 Polarization-induced charge and electron mobility in AlGaN/GaN heterostructures grown by plasma-assisted molecular-beam epitaxy *J. Appl. Phys.* **86** 4520–6

[69] Chen J T, Hsu C W, Forsberg U and Janzen E 2015 Metalorganic chemical vapor deposition growth of high-mobility AlGaN/AlN/GaN heterostructures on GaN templates and native GaN substrates *J. Appl. Phys.* **117** 085301

[70] Keller S, Parish G, Fini P T, Heikman S, Chen C H, Zhang N, DenBaars S P, Mishra U K and Wu Y F 1999 Metalorganic chemical vapor deposition of high mobility AlGaN/GaN heterostructures *J. Appl. Phys.* **86** 5850–7

[71] Wang X F, Yu R M, Jiang C Y, Hu W G, Wu W Z, Ding Y, Peng W B, Li S T and Wang Z L 2016 Piezotronic effect modulated heterojunction electron gas in AlGaN/AlN/GaN heterostructure microwire *Adv. Mater.* **28** 7234–8

[72] Bykhovski A D, Gaska R and Shur M S 1998 Piezoelectric doping and elastic strain relaxation in AlGaN–GaN heterostructure field effect transistors *Appl. Phys. Lett.* **73** 3577–9

[73] Sacconi F, Di Carlo A, Lugli P and Morkoc H 2001 Spontaneous and piezoelectric polarization effects on the output characteristics of AlGaN/GaN heterojunction modulation doped FETs *IEEE Trans. Electron Device* **48** 450–7

[74] Mishra U K, Parikh P and Wu Y F 2002 AlGaN/GaN HEMTs—an overview of device operation and applications *Proc. IEEE* **90** 1022–31

[75] Lee K S, Yoon D H, Bae S B, Park M R and Kim G H 2002 Self-consistent subband calculations of AlGaN/GaN single heterojunctions *ETRI J.* **24** 270–9

[76] Asgari A, Kalafi M and Faraone L 2005 A quasi-two-dimensional charge transport model of AlGaN/GaN high electron mobility transistors (HEMTs) *Physica* E **28** 491–9

[77] Osinski M, Smagley V A, Lu M, Smolyakov G A, Eliseev P G, Riely B P, Shen P H and Simonis G J 2003 Self-consistent calculation of current self-distribution effect in GaAs–AlGaAs oxide-confined VCSELs *IEEE J. Sel. Top. Quantum Electron.* **9** 1422–30

[78] Lenka T R and Panda A K 2011 Self-consistent subband calculations of $Al_xGa_{1-x}N$/(AlN)/GaN-based high electron mobility transistor *Adv. Mater. Res.* **159** 342–7